

1 **West Antarctic Ice Sheet retreat in the Amundsen Sea driven by decadal oceanic variability**

2 Adrian Jenkins^{1*}, Deb Shoosmith¹, Pierre Dutrieux², Stan Jacobs², Tae Wan Kim³, Sang Hoon Lee³, Ho
3 Kyung Ha⁴ & Sharon Stammerjohn⁵

4 ¹British Antarctic Survey, Natural Environment Research Council, Cambridge CB3 0ET, U.K.

5 ²Lamont-Doherty Earth Observatory of Columbia University, Palisades, NY 10964, U.S.A.

6 ³Korea Polar Research Institute, Incheon 406-840, Korea.

7 ⁴Department of Ocean Sciences, Inha University, Incheon 22212, Korea.

8 ⁵Institute of Arctic and Alpine Research, University of Colorado, Boulder, CO 80309, U.S.A.

9

10 **Mass loss from the Amundsen Sea sector of the West Antarctic Ice Sheet has increased in recent**
11 **decades, suggestive of sustained ocean forcing or ongoing, possibly unstable response to a past**
12 **climate anomaly. Lengthening satellite records appear incompatible with either process,**
13 **however, revealing both periodic hiatuses in acceleration and intermittent episodes of thinning.**
14 **Here we use ocean temperature, salinity, dissolved-oxygen and current measurements taken from**
15 **2000-2016 near Dotson Ice Shelf to determine temporal changes in net basal melting. A decadal**
16 **cycle dominates the ocean record, with melt changing by a factor of ~4 between cool and warm**
17 **extremes via a non-linear relationship with ocean temperature. A warm phase that peaked**
18 **around 2009 coincided with ice shelf thinning and retreat of the grounding line, which re-**
19 **advanced during a post-2011 cool phase. Those observations demonstrate how discontinuous ice**
20 **retreat is linked with ocean variability, and that the strength and timing of decadal extremes is**
21 **more influential than changes in the longer-term mean state. The non-linear response of melting**
22 **to temperature change heightens the sensitivity of Amundsen Sea ice shelves to such variability,**
23 **possibly explaining the vulnerability of the ice sheet in that sector, where subsurface ocean**
24 **temperatures are relatively high.**

25

26 The West Antarctic Ice Sheet (WAIS) has recently been contributing $\sim 0.3 \text{ mm yr}^{-1}$ to global sea level
27 rise¹, with the potential to discharge ice more rapidly into the ocean where its bed slopes downward
28 inland to as much as 2.5 km below sea level at its centre². That configuration can be inherently
29 unstable³ unless floating ice shelves at its margin provide sufficient restraint on ice discharge across
30 the grounding line^{4,5}. Since buttressing is generated where ice shelves contact lateral margins and
31 seabed shoals, ice shelf thinning reduces buttressing, accelerating the outflow of grounded ice⁶, a
32 process that makes the WAIS highly sensitive to ocean conditions at its margin. Understanding the
33 physical links between oceanic change and ice loss is thus critical to assessing the future of WAIS,
34 and the potential reversibility of recent changes.

35 Satellite observations provide a consistent picture of mass loss from West Antarctica's Amundsen
36 Sea sector over recent decades^{1,7,8,9}. Flow acceleration of outlet glaciers⁷ has been accompanied by
37 inland thinning^{1,9} and retreat of grounding lines⁸, while lengthening records have revealed elevated
38 rates of mass loss in recent years^{1,7}. Key outlet glaciers are buttressed only by small ice shelves¹⁰
39 that are furthermore exposed to relatively warm seawater¹¹. The thinning signature propagates
40 inland from grounding lines⁹, with downstream ice shelves thinning faster¹², pointing to changes in
41 buttressing triggered by ocean-driven melting as the cause.

42 Most studies have attributed the mass loss either to unstable retreat of the grounding lines^{13,14},
43 possibly triggered by a climate anomaly in the 1940s (15), or to sustained ocean forcing resulting
44 from a past increase in the quantity of warm water on the continental shelf¹⁶ or a long-term
45 warming of those waters¹⁷. Recent observations^{7,8,9} are, however, irreconcilable with such
46 hypotheses. Alternating phases of rapid acceleration and steady or even decelerating flow are
47 mostly coherent across different glaciers⁷. If all were retreating unstably or under sustained forcing,
48 variations in the rate of change would be dictated by the geometry and flow regime of individual
49 glaciers, and incoherent. Furthermore, current episodes of rapid thinning commenced on Pine
50 Island and Thwaites glaciers less than 30 years ago⁹, excluding a simple link with events in the 1940s.

51 Oceanographic records remain short and patchy on the Amundsen Sea continental shelf, where the
52 first full-depth profiles of seawater properties in the early 1990s revealed warm derivatives of
53 Circumpolar Deep Water in deep, glacially-scoured troughs and a consequent high melt rate beneath
54 Pine Island Ice Shelf¹¹. Subsequent summer cruises indicated that Pine Island melt rates tracked
55 ocean heat content, increasing between 1994 and 2009 (18) and decreasing between 2010 and 2012
56 (19). The cool phase persisted for several years²⁰, causing deceleration of the glacier that has
57 typically been interpreted as a minor perturbation to the long-term retreat^{21,22}. Getz Ice Shelf
58 experienced a more pronounced change in melting between cool ocean conditions in 2000 and
59 warm in 2007 (23), but the inland ice response remains undocumented. For both ice shelves, ship-
60 based measurements have been limited by persistent sea ice fields, but near-repeat stations
61 throughout the Amundsen continental shelf indicate spatially coherent cool and warm periods²⁴.

62 **Melt rates inferred from observation at Dotson Ice Front**

63 In this region, the most reliable area of summer open water is the Amundsen Sea Polynya, which
64 forms to the north of Dotson and eastern Getz ice shelves. Ships have thus been able to access that
65 area more often, yielding eight near-repeat sets of seawater properties close to Dotson Ice Front
66 from 2000-2016 (Figure 1). Combining those observations shows how Dotson basal melting has
67 evolved in response to changing ocean conditions.

68 The ice front water column comprises two relatively uniform layers separated by a region with
69 higher vertical thermohaline gradients (Figure 2). The warmer and saltier bottom layer (typically
70 near 0.5°C and 34.55), is derived from modified Circumpolar Deep Water (mCDW) that flows onto
71 the shelf near 118°W and circulates cyclonically within the Dotson-Getz Trough^{25,26}. The colder,
72 fresher upper layer (typically near -1.25°C and 33.8) is derived from Winter Water (WW), formed as
73 a result of cooling, brine drainage and convection beneath growing sea ice, and having properties
74 that vary mainly through the degree of summer warming and the depth of winter mixing. The
75 bottom layer stands out for being coldest in 2000, but more striking temperature changes occur near

76 the mid-depth transition region between the two layers (Figure 2). When that thermocline is
77 shallow (deep), significantly more (less) ocean heat is available to melt ice within the sub-Dotson
78 cavity. Deep thermoclines in 2000 and 2012-2016 bracket shallower levels in 2006-2011, changes
79 that are coherent with less complete records elsewhere^{18,19,23}, albeit with systematic spatial
80 differences²⁴.

81 After calculating seawater density from temperature and salinity, those parameters are used to
82 determine the circulation and transport of meltwater across the ice front (Methods). In years when
83 ocean current profiles were directly measured, their combination with seawater properties yields
84 independent estimates of circulation and melting. A persistent east side inflow that is warmer and
85 deeper than west side outflow is consistent with the addition of meltwater from the ice shelf base
86 driving a geostrophic circulation (Figure 3). More variable transports appear elsewhere across the
87 section.

88 Estimates of the net meltwater flux across the sections closely track variations in mean temperature
89 above freezing associated with changes in thermocline depth (Figure 4a). Both quantities are
90 estimated using observations over the entire section, but exclude a variable-depth surface layer
91 where air-sea interaction influences the water properties (Methods). Meltwater fluxes were ~4
92 times higher at the peak warm phase in 2009 than during cool phases before and after, when values
93 were similar despite the change in deep temperature maximum (Figure 2a). Intermediate melt rates
94 in 2006 and 2007 are consistent with a glaciological estimate²⁷ derived from 2003-2008 satellite data
95 (Figure 4a). Satellite-based estimates of spatial²⁸ and temporal^{29,30} variability in Dotson Ice Shelf
96 melting combine ice thicknesses derived from surface elevation data, a procedure that magnifies
97 uncertainties by an order of magnitude, with surface accumulation and firn compaction rates
98 derived from models that lack independent verification²⁹ or assumed constant³⁰. Although subject
99 to their own methodological uncertainty, our estimates are independent of regional climate models
100 and assumptions about firn density.

101 **Ice sheet changes driven by melt rate variability**

102 The 16-year history of melting explains the recently-observed behaviour of Dotson Ice Shelf and its
103 tributary ice streams, especially Kohler Glacier (Figure 4b). Surface accumulation and iceberg calving
104 make small, mutually-cancelling contributions to the Dotson mass budget²⁷, so when melt equals ice
105 flux across the grounding line the ice shelf is close to equilibrium. The low, near-equilibrium melt
106 rate in 2000 was followed by 4 years of steady ice influx⁷. A period of rapid acceleration⁷, thinning³¹,
107 and grounding line retreat⁸ then occurred from 2004-2011, when melt rates significantly exceeded
108 equilibrium values. A cooler interval beginning in 2012 caused a steadying of the flow⁷ and re-
109 advance of the Kohler Glacier grounding line⁸, as melting dropped below the now-elevated
110 equilibrium value.

111 Such behaviour provides insight into the physical processes that link ocean forcing with ice sheet
112 response. Thermocline shoaling induces thinning of the ice shelf, reducing its contact with margins
113 and seabed, and weakening buttressing at the grounding line⁶, where flow accelerates in response⁷.
114 Consequent thinning of inland ice causes retreat of the grounding line⁸, further reducing local
115 resistance to flow³², and steepens the slope of the glacier surface, increasing local forcing of the
116 flow³³. Those secondary effects induce further acceleration, and develop over time at a rate that is
117 determined by the glacier bed and margin geometries, and the local resistance they provide to the
118 flow⁹. Subsequent deepening of the thermocline reduces melting, causing ice shelf thickening and
119 increased buttressing at the new grounding line. Inland response is now complicated by a
120 continuing adjustment of ice thickness and flow to the earlier perturbation.

121 The non-linear relationship between meltwater flux and mean seawater temperature (Figure 4c)
122 confirms theoretical inferences wherein turbulent ice-ocean heat transfer depends on both the
123 temperature difference across the boundary layer and the shear generated by the far-field
124 geostrophic current, itself driven by temperature-related density differences (Methods). A similar
125 relationship exists in numerical models of sub-ice circulation applied to idealised ice and seabed

126 geometries³⁴. That non-linearity has important implications for ice shelf vulnerability to changing
127 ocean conditions, enhancing melt rate sensitivity as the mean state temperature rises. For a given
128 temperature increase, ice shelves will thin more rapidly in the warm SE Pacific sector than elsewhere
129 on the Antarctic continental shelf, where subsurface seawater temperatures are typically closer to
130 the surface freezing point.

131 **Ocean variability as a driver of change in the Amundsen Sector**

132 Models and observations give a consistent picture of winds over the continental shelf as the main
133 driver of thermocline depth variability and consequent changes in melting throughout the eastern
134 Amundsen Sea^{22,35,36}. Various processes including wind-forced variability of mCDW inflow³⁷ and
135 near-coastal densification^{20,38} and downwelling of WW³⁹ have been invoked. If critical wind changes
136 are associated with regional circulation anomalies triggered from the tropical Pacific^{29,40}, forcing
137 during prior decades would have been characterised by similar cycles²². Coupled with the non-linear
138 response of ice shelf melting, such pronounced variability makes the Amundsen Sea sector of the
139 WAIS particularly susceptible to decadal changes in ice shelf buttressing.

140 The region-wide observations of intermittent acceleration⁷ and more sustained, but episodic
141 thinning⁹ are explicable in terms of such forcing (Figure 5). Warm phases are characterised by rapid
142 acceleration in ice flow, as ice shelves thin and buttressing decreases. Flow steadies or decelerates
143 during cool phases, with exceptions because individual glacier bed geometry determines the size of
144 the evolving inland response to the preceding acceleration. The resilience of Kohler Glacier through
145 the recent period of elevated melting beneath Dotson Ice Shelf indicates that a grounding line
146 pinned on a prominent seabed rise⁸ can limit the response to reduced buttressing and allow
147 recovery during a subsequent cool phase. With a less stable grounding line, acceleration resulting
148 from reduced buttressing can initiate a short period of unstable retreat, triggering an inland-
149 propagating wave of thinning⁹, and further acceleration that may over-ride a cooling-induced
150 increase in ice shelf buttressing. Evidence (Figure 5) suggests that episodes of retreat occurred in

151 the 1940s, the 1970s and the 1990s on Pine Island Glacier^{9,15}, in the early 2000s on Thwaites and
152 Haynes glaciers⁹, and with less certain timing on the glaciers feeding Dotson and Crosson ice
153 shelves⁹.

154 Longer-term change may underlie the pronounced decadal variability reported here. That might
155 account for the mean ocean state over the 2000-2016 period being warm enough to induce thinning
156 of Dotson Ice Shelf (Figure 4b). However, inland thinning of Kohler Glacier⁹ indicates a retreat
157 episode prior to 2000 (Figure 5). Associated deepening of the grounding line would have exposed
158 more of the ice shelf base to the warmer mCDW, elevating the melt rate for equivalent ocean
159 forcing. The absence of significant inland thinning on Pine Island Glacier prior to the 1990s retreat⁹
160 suggests that a near-equilibrium state was re-established there following major perturbations in the
161 1940s and 1970s (15).

162 It now appears that recent accelerated mass loss from the Amundsen Sea sector of the WAIS has not
163 resulted from progressive ocean warming or unstable ice retreat, but rather from a combination of
164 analogous processes whereby successive warm intervals trigger episodic retreats of the most
165 vulnerable grounding lines, adding to a longer-term inland response. Over recent decades, pauses in
166 acceleration and minor decelerations in Amundsen Sea outlet glaciers during cool periods (Figure 5)
167 may have reduced the rate of ice loss from West Antarctica, as documented since 2011 for the
168 current cool phase⁴¹. Determining the magnitude of committed loss from past and future warm
169 episodes will require better understanding of ice shelf and outlet glacier response to, and the origins
170 of, the strong temporal variability of the mid-depth thermocline that dominates the recent record of
171 shelf water properties.

172

173 **References**

- 174 1. Shepherd, A. et al. A reconciled estimate of ice-sheet mass balance. *Science* **338**, 1183–1189
175 (2012).
- 176 2. Fretwell, P. et al. Bedmap2: improved ice bed, surface and thickness datasets for Antarctica. *The*
177 *Cryosphere* **7**, 375–393 (2013).
- 178 3. Schoof, C. Ice sheet grounding line dynamics: steady states, stability, and hysteresis. *J. Geophys.*
179 *Res.* **112**, F03S28 (2007).
- 180 4. Goldberg, D., Holland, D.M. & Schoof, C. Grounding line movement and ice shelf buttressing in
181 marine ice sheets. *J. Geophys. Res.* **114**, F04026 (2009).
- 182 5. Gudmundsson, G.H. 2013. Ice-shelf buttressing and the stability of marine ice sheets. *The*
183 *Cryosphere* **7**, 47–655 (2013).
- 184 6. Reese, R., Gudmundsson, G.H., Levermann, A. & Winkelmann, R. The far reach of ice-shelf
185 thinning in Antarctica. *Nat. Clim. Change* **8**, 53–57 (2018).
- 186 7. Mouginot, J., Rignot, E., & Scheuchl, B. Sustained increase in ice discharge from the Amundsen
187 Sea Embayment, West Antarctica, from 1973 to 2013. *Geophys. Res. Lett.* **41**, 1576–1584 (2014).
- 188 8. Scheuchl, B., Mouginot, J., Rignot, E., Morlighem, M., & Khazendar A. Grounding line retreat of
189 Pope, Smith, and Kohler Glaciers, West Antarctica, measured with Sentinel-1a radar interferometry
190 data. *Geophys. Res. Lett.* **43**, 8572–8579 (2016).
- 191 9. Konrad, H. et al. Uneven onset and pace of ice-dynamical imbalance in the Amundsen Sea
192 Embayment, West Antarctica. *Geophys. Res. Lett.*, **44**, 910–918 (2017).
- 193 10. Thomas, R.H., Sanderson, T.J.O. & Rose, K.E. Effect of climatic warming on the West Antarctic ice
194 sheet. *Nature* **277**, 355–358 (1979).
- 195 11. Jacobs, S.S., Hellmer, H.H. & Jenkins, A. Antarctic ice sheet melting in the southeast Pacific.
196 *Geophys. Res. Lett.* **23**, 957–960 (1996).

- 197 12. Paolo, F.S., Fricker, H.A. & Padman, L. Volume loss from Antarctic ice shelves is accelerating.
198 *Science* **348**, 327–331 (2015).
- 199 13. Favier, L. et al. Retreat of Pine Island Glacier controlled by marine ice-sheet instability. *Nat. Clim.*
200 *Change* **4**, 117–121 (2014).
- 201 14. Joughin, I., Smith, B.E. & Medley, B. Marine Ice Sheet Collapse Potentially Under Way for the
202 Thwaites Glacier Basin, West Antarctica. *Science* **344**, 735–738 (2014).
- 203 15. Smith, J.A. et al. Sub-ice shelf sediments record 20th Century retreat history of Pine Island
204 Glacier. *Nature* **541**, 77–80 (2017).
- 205 16. Hillenbrand, C.-D. et al. West Antarctic Ice Sheet retreat driven by Holocene warm water
206 incursions. *Nature* **547**, 43–48 (2017).
- 207 17. Schmidtko, S., Heywood, K.J., Thompson, A.F. & Aoki, S. Multidecadal warming of Antarctic
208 waters. *Science* **346**, 1227–1231 (2014).
- 209 18. Jacobs, S.S., Jenkins, A., Giulivi, C.F. & Dutrieux, P. Stronger ocean circulation and increased
210 melting under Pine Island Glacier ice shelf. *Nat. Geosci.* **4**, 519–523 (2011).
- 211 19. Dutrieux, P. et al. Strong sensitivity of Pine Island Ice-Shelf melting to climatic variability. *Science*
212 **343**, 174–178 (2014).
- 213 20. Webber, B.G.M. et al. Mechanisms driving variability in the ocean forcing of Pine Island Glacier.
214 *Nat. Commun.* **7**, 14507 (2017).
- 215 21. Christianson, K. et al. Sensitivity of Pine Island Glacier to observed ocean forcing, *Geophys. Res.*
216 *Lett.* **43**, 10,817–10,825 (2016).
- 217 22. Jenkins, A. et al. Decadal ocean forcing and Antarctic Ice Sheet response: lessons from the
218 Amundsen Sea. *Oceanography* **29**(4), 106–117 (2016).

- 219 23. Jacobs, S. et al. Getz Ice Shelf melting response to changes in ocean forcing, *J. Geophys. Res.*
220 *Oceans* **118**, 4152–4168 (2013).
- 221 24. Jacobs, S. et al. The Amundsen Sea and the Antarctic Ice Sheet, *Oceanography* **25**, 154–163
222 (2012).
- 223 25. Wåhlin, A.K., Yuan, X., Björk, G. & Nohr, C. Inflow of warm Circumpolar Deep Water in the
224 central Amundsen shelf. *J. Phys. Oceanogr.* **40**, 1427–1434 (2010).
- 225 26. Ha, H.K. et al. Circulation and Modification of Warm Deep Water on the Central Amundsen
226 Shelf. *J. Phys. Oceanogr.* **44**, 1493–1501 (2014).
- 227 27. Rignot, E., Jacobs, S., Mouginot, J., & Scheuchl, B. Ice-shelf melting around Antarctica. *Science*
228 **341**, 266–270 (2013).
- 229 28. Gourmelen, N. et al. Channelized melting drives thinning under a rapidly melting Antarctic ice
230 shelf. *Geophys. Res. Lett.* **44**, 9796–9804 (2017).
- 231 29. Paolo, F.S. et al. Response of Pacific-sector Antarctic ice shelves to the El Niño/Southern
232 Oscillation. *Nat. Geosci.* **11** (2018).
- 233 30. Lilien, D.A., Joughin, I., Smith, B. & Shean, D.E. Changes in flow of Crosson and Dotson ice
234 shelves, West Antarctica, in response to elevated melt, *The Cryosphere* **12**, 1415–1431 (2018).
- 235 31. Khazendar, A. et al. Rapid submarine ice melting in the grounding zones of ice shelves in West
236 Antarctica. *Nat. Commun.* **7**, 13243 (2016).
- 237 32. Payne, A.J., Vieli, A., Shepherd A.P., Wingham, D.J. & Rignot, E. Recent dramatic thinning of
238 largest West Antarctic ice stream triggered by oceans, *Geophys. Res. Lett.* **31**, L23401 (2004).
- 239 33. Scott, J.B.T. et al. Increased rate of acceleration on Pine Island Glacier strongly coupled to
240 changes in gravitational driving stress, *The Cryosphere* **3**, 125–131 (2009).

- 241 34. Holland, P.R., Jenkins, A. & Holland, D.M. The response of ice shelf basal melting to variations in
242 ocean temperature. *J. Climate* **21**, 2558–2572 (2008).
- 243 35. Kimura, S. et al. Oceanographic controls on the variability of ice-shelf basal melting and
244 circulation of glacial meltwater in the Amundsen Sea Embayment, Antarctica. *J. Geophys. Res.*
245 *Oceans* **122**, in press (2017).
- 246 36. Turner, J. et al. Atmosphere-ocean-ice interactions in the Amundsen Sea Embayment, West
247 Antarctica. *Rev. Geophys.* **55**, 235–276 (2017).
- 248 37. Thoma, M., Jenkins, A., Holland, D. & Jacobs, S. Modelling Circumpolar Deep Water intrusions on
249 the Amundsen Sea continental shelf, Antarctica. *Geophys. Res. Lett.* **35**, L18602 (2008).
- 250 38. St-Laurent, P., Klinck, J.M. & Dinniman, M.S. Impact of local winter cooling on the melt of Pine
251 Island Glacier, Antarctica. *J. Geophys. Res. Oceans* **120**, 6718–6732 (2015).
- 252 39. Kim, C.S. et al. Is Ekman pumping responsible for the seasonal variation of warm circumpolar
253 deep water in the Amundsen Sea? *Cont. Shelf Res.* **132**, 38–48 (2017).
- 254 40. Steig, E.J., Ding, Q., Battisti, D.S. & Jenkins, A. Tropical forcing of Circumpolar Deep Water inflow
255 and outlet glacier thinning in the Amundsen Sea Embayment, West Antarctica. *Ann. Glaciol.* **53**(60),
256 19–28 (2012).
- 257 41. The IMBIE Team. Mass balance of the Antarctic Ice Sheet from 1992 to 2017. *Nature* **558**, 219–
258 222 (2018).

259

260 **Acknowledgements**

261 We are grateful to all cruise participants who assisted in the collection of the data. AJ and DS were
262 supported by core funding from the UK Natural Environment Research Council (NERC) to the British
263 Antarctic Survey's Polar Oceans Program. PD was supported by funding from NERC's iSTAR

264 Programme through grant NE/J005770/11 and NSF grant 1643285. SJ support included NSF grants
265 ANT06-32282 and 16-44159. Support for SHL and TWK was provided by the Korea Polar Research
266 Institute grant KOPRI PE17060. SS was supported by National Science Foundation Office of Polar
267 Programs collaborative grants 0838975 and 1443569.

268 **Author contributions**

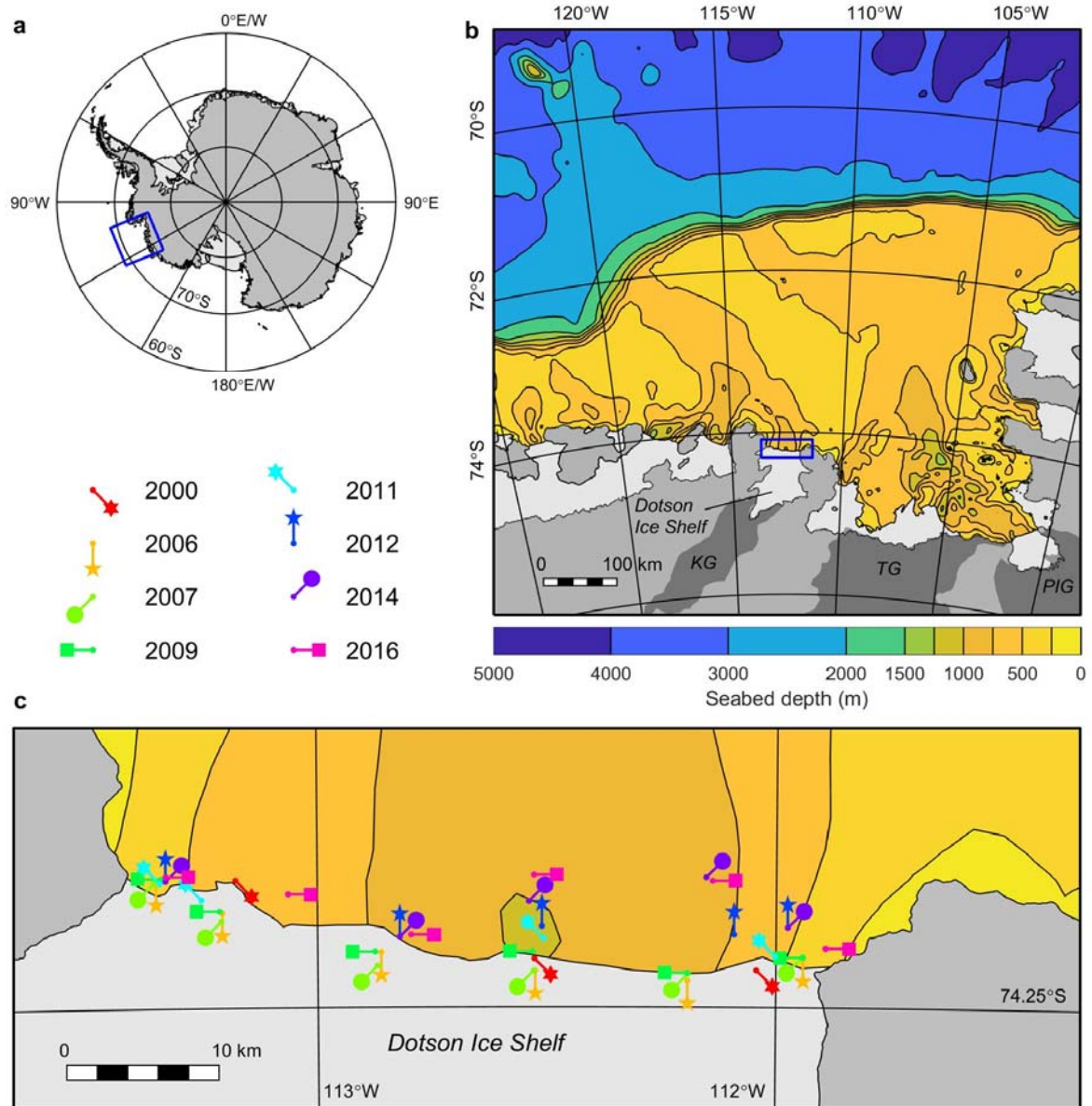
269 AJ, DS, PD and SJ conceived the study. DS, SJ, TWK, SHL, HKH and SS planned and led the data
270 collection. DS, PD, and TWK processed the data. AJ, DS and PD undertook the data analyses and
271 derivation of the final results. AJ prepared the manuscript. All authors discussed the results and
272 implications and commented on the manuscript at all stages.

273 **Competing financial interests**

274 The authors declare no competing financial interests.

275 **Materials and correspondence**

276 Correspondence and material requests should be addressed to A. Jenkins (ajen@bas.ac.uk), or to the
277 contacts listed in Supplementary Table 1 for more specific cruise information.



278

279

Figure 1 | Locations of Amundsen Sea observations used in this study. (a) Map of Antarctica

280

indicating grounded ice sheet (darker shading), floating ice shelves (lighter shading) and study area

281

(blue box). (b) Enlargement of study area showing regional bathymetry² and catchments (darker

282

shading) of Kohler, Thwaites and Pine Island glaciers (KG, TG, PIG).

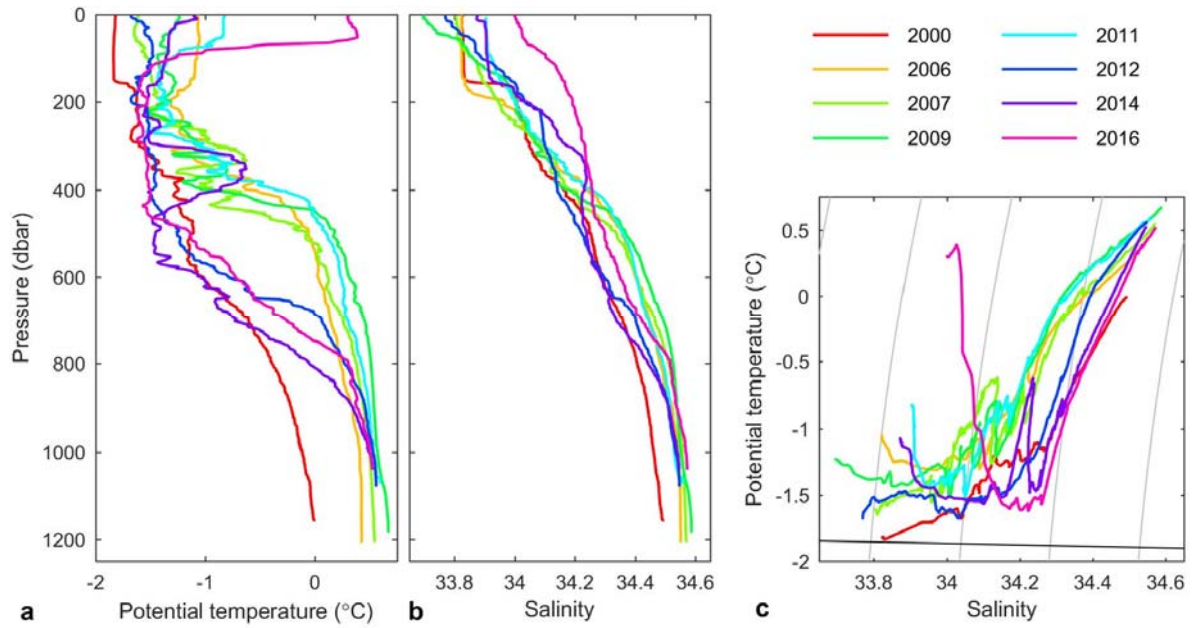
283

enlargement of area near the moving Dotson Ice Front (blue box in panel b) showing locations and years of summer (Dec-Mar)

284

vertical profiles of seawater properties.

285

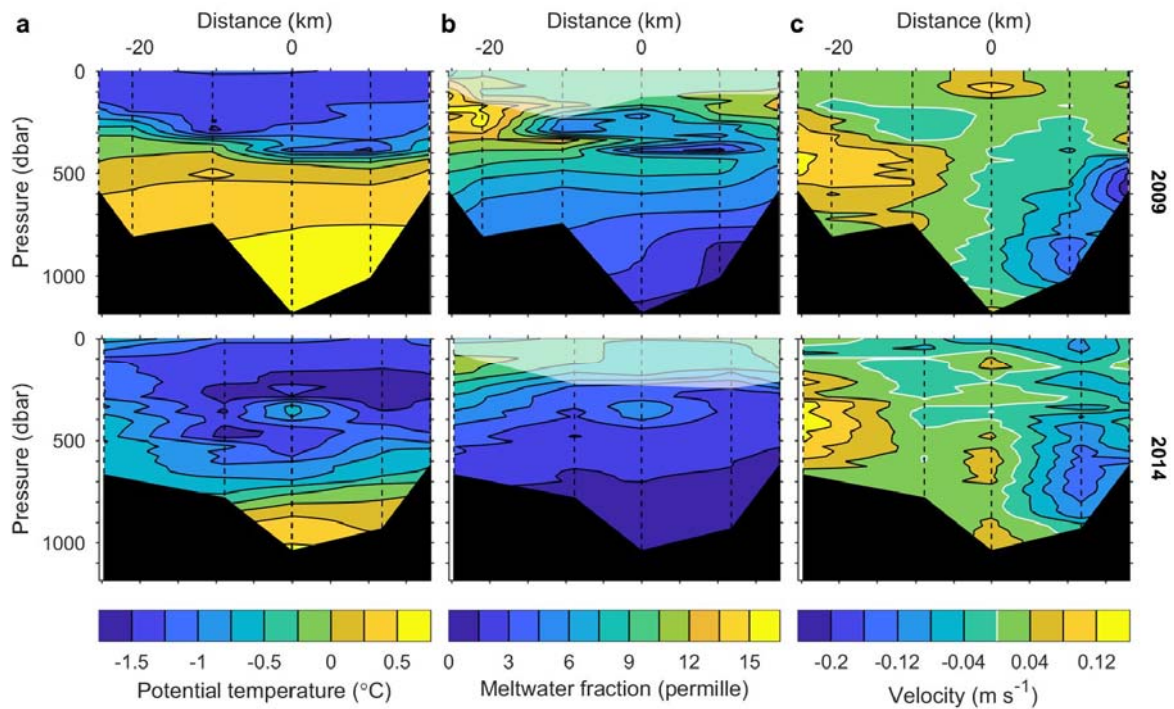


286

287 **Figure 2 | Potential temperature and salinity at Dotson Ice Front.** (a) Vertical profiles of potential
 288 temperature recorded at the deepest station sampled in each summer; near-repeats, centrally
 289 located in the trough near 112.5°W (Figure 1c). (b) Vertical profiles of salinity recorded at the same
 290 stations. (c) Potential temperature versus salinity for the stations in panels a and b. Grey lines
 291 connect points of equal potential density (1027 to 1027.8 kg m^{-3} in 0.2 kg m^{-3} increments), while the
 292 black line indicates the surface freezing point.

293

294



295

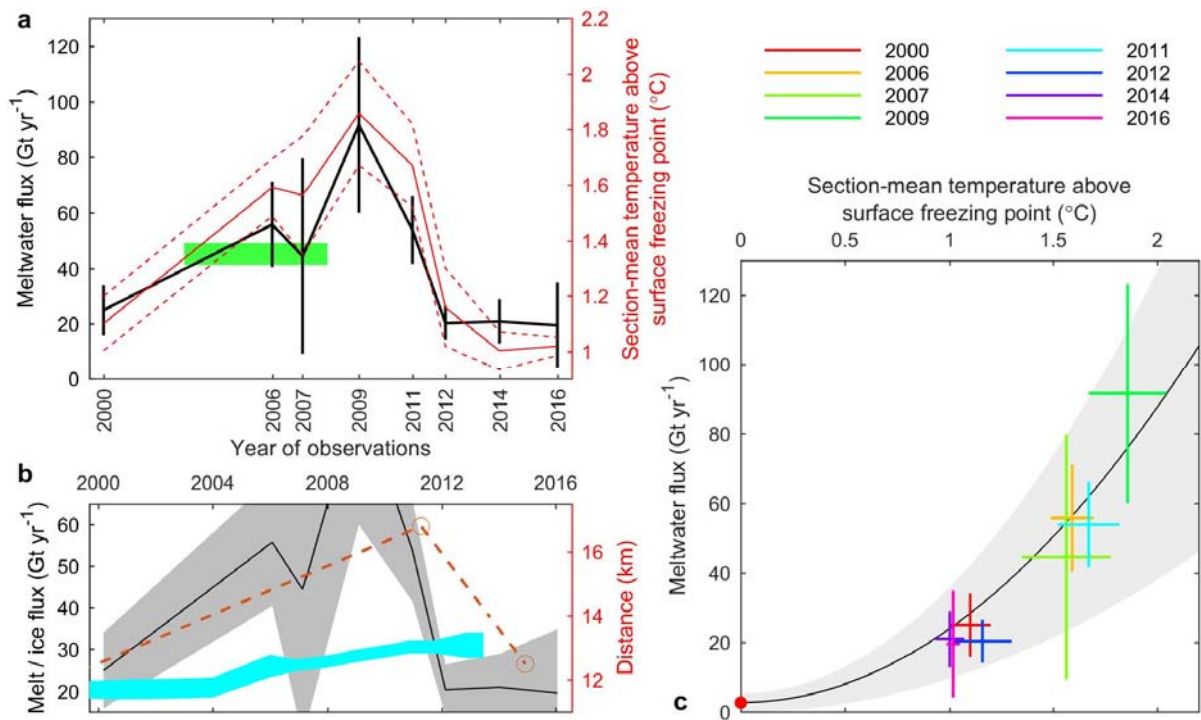
296 **Figure 3 | Cross-sections of potential temperature, meltwater fraction and current speed**

297 **perpendicular to the ice front in contrasting years.** (a) Potential temperature at stations (vertical
 298 dashed lines) in 2009 (top) and 2014 (bottom). Distance relative to the central trough station (Figure
 299 2) is positive eastward, and black shading shows the seabed, linearly interpolated between stations.

300 (b) Meltwater fraction derived from potential temperature, salinity and dissolved oxygen
 301 concentration (Methods), lighter where the calculation is unreliable due to the influence of air-sea
 302 interactions. (c) Lowered Acoustic Doppler Current Profiler speeds perpendicular to the ice front,
 303 positive for northward outflows.

304

305

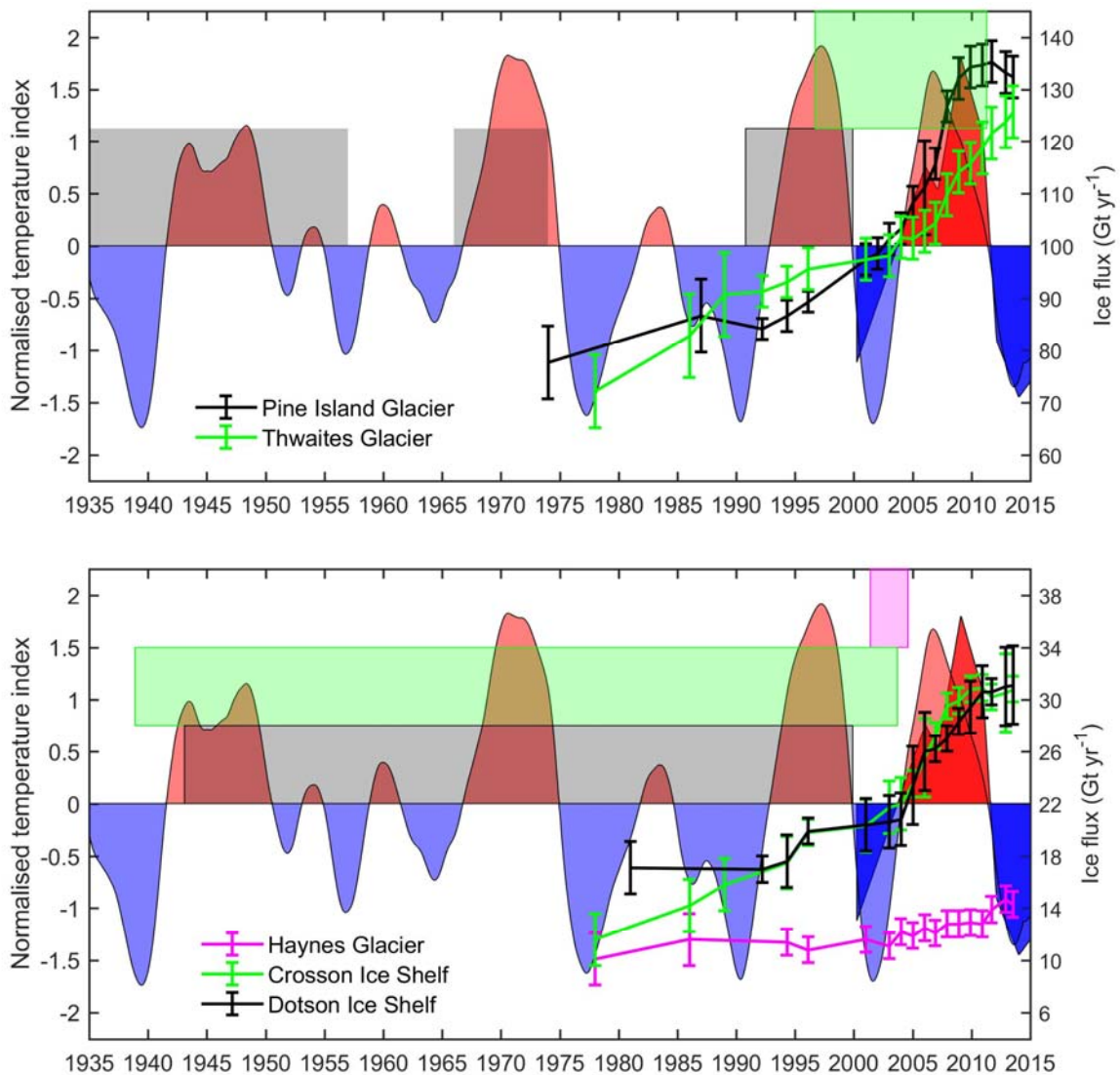


306

307 **Figure 4 | Meltwater flux and mean ocean temperature at Dotson Ice Front.** (a) Time series of
 308 meltwater flux (black, one standard deviation bars) and mean temperature above the surface
 309 freezing point (red, one standard deviation dashed lines), with melt flux derived from 2003-2008
 310 satellite data²⁷ (green). (b) Meltwater flux (black), mass flux across Dotson Ice Shelf grounding line⁷
 311 (cyan) and relative position of Kohler Glacier grounding line⁸ (red). (c) Meltwater flux versus mean
 312 temperature above the surface freezing point (colour-coded by year). The black line is a theoretical
 313 quadratic relationship (Methods) with uncertainties (grey shading), using an additional point (red
 314 dot) estimated from observations in cold water sectors of Antarctica²⁷.

315

316



317

318 **Figure 5 | Multi-decadal history of ocean forcing and outlet glacier response in the eastern**

319 **Amundsen Sea.** Time series of glacier outflow changes⁷ (right-hand axis) and ocean forcing (red =
 320 warm conditions; blue = cool conditions) as documented here (darker shading) and inferred (lighter
 321 shading) from central tropical Pacific sea surface temperatures²² (left-hand axis, both normalised).
 322 Shaded boxes (outlined and colour-coded by glacier) indicate the range of estimated times for the
 323 initiation of the most recent phase of rapid thinning at the grounding lines⁹, while boxes without
 324 outlines are inferred times of initial and final detachment of Pine Island Glacier from a submarine
 325 ridge¹⁵.

326 **Methods**

327 ***Data collection***

328 Data were collected from three marine research vessels during eight summer visits to the Amundsen
329 Sea (Supplementary Table 1). All cruises used Sea-Bird Scientific SBE 911plus Conductivity-
330 Temperature-Depth (CTD) profiling systems, with consistent recording and processing procedures.
331 On seven cruises, dissolved oxygen (DO) sensors were added to the system, and on five, Lowered
332 Acoustic Doppler Current Profilers (LADCP) were mounted on the CTD frame. Scalar data were
333 averaged into 1- or 2-dbar pressure bins, while current data were averaged into larger bins of
334 typically 20 dbar. Most section profiles were regularly spaced within a few hundred metres of the
335 Dotson Ice Front (Figure 1 and Supplementary Figure 1).

336 ***Meltwater fraction calculations***

337 As ice melts into seawater the resulting water mass becomes cooler, fresher and richer in dissolved
338 oxygen than the original. Most of the cooling occurs because the seawater supplies the latent heat
339 required for the phase change, freshening because of the addition of meltwater, and dissolved
340 oxygen concentrations rise as air bubbles trapped in the ice go into solution. Any combination of
341 potential temperature, salinity and dissolved oxygen can be used to diagnose the meltwater content
342 as the third component of a mixture incorporating modified Circumpolar Deep Water (mCDW) and
343 Winter Water (WW) as the other end members⁴² (Supplementary Table 2). Ice properties are
344 assumed to be constant, whereas mCDW and WW properties are cruise specific and are defined by
345 reference to the distribution of data in property-property plots (Supplementary Figure 2).

346 In property-property space, the data lie within a triangle defined by straight lines originating from
347 the mCDW properties⁴². One line connects the mCDW and ice end points and indicates seawater
348 properties that arise from ice melting into “pure” mCDW. A second line connecting mCDW and WW
349 end points represents properties that arise from mixing between the “pure” WW and mCDW.

350 Mixtures on the second line contain no meltwater and define the “ambient” water column that
351 interacts with the ice. The distance that a point lies from the “ambient” line indicates the meltwater
352 content that can be quantified as⁴²:

$$353 \quad \phi = \frac{(\chi^2 - \chi_{mCDW}^2) - (\chi^1 - \chi_{mCDW}^1) (\chi_{WW}^2 - \chi_{mCDW}^2) / (\chi_{WW}^1 - \chi_{mCDW}^1)}{(\chi_{ICE}^2 - \chi_{mCDW}^2) - (\chi_{ICE}^1 - \chi_{mCDW}^1) (\chi_{WW}^2 - \chi_{mCDW}^2) / (\chi_{WW}^1 - \chi_{mCDW}^1)}$$

354 where ϕ is the meltwater fraction, χ^i represents any of potential temperature, salinity or dissolved
355 oxygen, and subscripts indicate defined water mass properties (Supplementary Table 2).

356 WW is formed when heat loss to the atmosphere causes freezing at the sea surface. As the sea ice
357 grows, salt is rejected from the solid phase, increasing surface water salinity and driving convection.

358 The result is a deep mixed layer with a temperature at the surface freezing point and a salinity that
359 varies from year to year, depending on the amount and salinity of sea ice grown during the winter.

360 Formed by air-sea interaction at the surface, WW is rich in dissolved oxygen, but not necessarily
361 saturated as the consolidating ice cover presents a barrier to air-sea gas exchange. Since “pure”

362 WW, having a temperature at the surface freezing point, is absent from the summertime ice front

363 sections, we estimate a range of possible properties (Supplementary Table 2, Supplementary Figure

364 2) and investigate the sensitivity of results to that property range. The mCDW properties are

365 defined as the intersection between the ice/mCDW mixing line, which connects the ice properties

366 with one edge of the data “triangle”, and the WW/mCDW mixing line, which connects the mid-range

367 of the WW properties with the other edge of the data “triangle” (Supplementary Figure 2).

368 In some of the cold years we find that the mCDW properties thus defined do not correspond to the

369 warmest waters near the ice front, indicating a lack of direct interaction with the ice. This points to

370 recirculation deeper than the ice shelf draught, or exclusion from the inner cavity by a seabed

371 shoal⁴³, as on Pine Island Glacier^{44,45}. Heat from those waters could still contribute to melting if

372 mixed into the thermocline. In other years the mCDW properties are warmer and saltier than any

373 waters near the ice front, an indication that some seawater arriving at the ice front has formed from

374 ice melting into the warmer and saltier mCDW in Pine Island Bay²⁴. Those waters flow westward
375 along the continental shelf^{45,46} and carry meltwater beneath Dotson Ice Shelf.

376 Profiles of meltwater fraction, calculated using mid-range WW properties, are shown for all stations
377 in Supplementary Figure 3. Since interaction with the atmosphere can influence all three tracers,
378 the assumption of a three water mass mixture breaks down near the sea surface. In principle a
379 fourth, surface water mass could be defined, but in practice the surface properties are too spatially
380 heterogeneous to be defined as a single water mass. Instead we use the scatter of results derived
381 from the three separate calculations of meltwater fraction to indicate where atmospheric
382 interaction (or another process) makes the results unreliable (Supplementary Figure 3). This
383 exclusion will lower net melting estimates if cavity outflows are light enough to upwell into the
384 surface layer. Sections of potential temperature, salinity and dissolved oxygen are shown in
385 Supplementary Figure 1 and derived meltwater fractions are shown in Supplementary Figure 3.

386 ***Meltwater transport calculations***

387 The net flux of meltwater away from the ice shelf is calculated by combining estimates of meltwater
388 fraction and currents perpendicular to the ice front. While the latter can be observed directly, as
389 during some cruises (Supplementary Table 1), inherently large measurement uncertainties are
390 compounded by high-frequency variability associated with tides, waves and eddies that contaminate
391 the longer-term mean flow relevant to the calculation of meltwater transport. However, higher-
392 frequency processes have a smaller impact on the density structure derived from measurements of
393 temperature and salinity, of greater value in estimating the longer-term mean circulation⁴⁷.

394 At spatial scales larger than the local internal Rossby radius (a few kilometres) the pressure gradient
395 that drives the flow is balanced primarily by the Coriolis force it generates, allowing across-section
396 currents to be estimated from along-section pressure gradients. To make direct use of the pressure
397 recorded by the CTD, it is convenient to work in an isobaric framework, in which the geostrophic
398 currents can be derived from the slope of isobars relative to geopotential surfaces. As isobar depth

399 is the integral of specific volume (reciprocal of density) from the surface down to the relevant
400 pressure, relative isobar slope between any two stations can readily be derived from the CTD data.
401 Absolute isobar slope remains unknown because the slope of the sea surface relative to the geoid
402 cannot be precisely measured, introducing a pressure-independent unknown into the calculated
403 isobaric slopes. Calculated currents thus include a CTD-derived, pressure-dependent component,
404 and a pressure-independent component that must be estimated in some other way:

$$405 \quad v(P) = v(P_{ref}) + \frac{1}{f} \frac{\partial}{\partial x} \left(\int_P^{P_{ref}} \alpha dP \right) \Big|_P$$

406 where x is the along-section coordinate, v the across-section current, P is pressure, α is specific
407 volume, f the Coriolis parameter, and ref refers to an arbitrary reference pressure where the flow
408 associated with the absolute slope of the isobar must be determined⁴⁷.

409 The conventional solution is then to select a pressure level where it is physically reasonable to
410 assume the isobar is parallel to the geoid and hence the velocity is zero. For the Dotson Ice Front
411 sections, such a level of zero motion might be the maximum depth on each station at which
412 meltwater is found (Supplementary Figure 3). Zero motion at that level would be consistent with a
413 pure overturning circulation with warm inflow at depth and outflows of glacially-modified water at
414 shallower levels. Given the large scale of the ocean cavity beneath Dotson Ice Shelf compared with
415 the internal Rossby radius, we should anticipate a significant horizontal, geostrophic circulation
416 accompanying the overturning^{18,19}. The magnitude of the horizontal circulation can be estimated by
417 adapting a procedure for inferring reference level currents⁴⁸. Since the CTD sections completely
418 enclose a volume of the ocean, integral constraints on the circulation across the section can be
419 derived from the conservation of mass and scalar properties, along with a steady state assumption
420 within that volume. Flow between individual station pairs can then be adjusted by adding to each a
421 non-zero $v(P_{ref})$ that makes the overall circulation compatible with the constraints. With typically
422 fewer constraints than unknown reference velocities, yielding infinitely many solutions that satisfy

423 the constraints exactly, the adopted strategy is to choose the solution that minimises the sum of the
424 squares of the reference velocities (i.e. that is closest, in terms of the L_2 norm, to the original
425 circulation with zero reference velocities).

426 The next problem is that the conventional approach of imposing zero mass, heat and salt fluxes at
427 the ice front constrains the solution to give a net meltwater flux of zero across the section, in turn
428 requiring a novel strategy to overcome that limitation⁴⁷. Knowing the ice properties (Supplementary
429 Table 2), the impact of meltwater addition on all conservation equations (mass, heat, salt and
430 dissolved oxygen, where measured) can be quantified in terms of the yet-to-be-determined
431 meltwater flux. The mass conservation equation can then be used to eliminate the unknown melt
432 rate from the other equations. The system yields as many constraints as there are tracers observed,
433 effectively balancing the budgets associated with the circulation of meltwater-free source waters,
434 and the resulting imbalance between total inflow and outflow is the sought-after meltwater flux
435 (Supplementary Table 3). Another estimate of the meltwater flux can be obtained from the net
436 transport of meltwater fraction, quantified as described above, associated with the derived
437 circulation. Both estimates yield the net meltwater flux across the section, with the latter
438 additionally giving the meltwater concentration in the inflow that is sourced from elsewhere
439 (Supplementary Table 3) and the total in the outflow. The two estimates of the melt added from the
440 ice shelf are independent, since the first requires only that integrated inflow and integrated outflow
441 properties be connected by a meltwater mixing line. It is thus formally independent of the choice of
442 WW and mCDW properties, although indirect use is made of the scatter in meltwater fraction
443 calculations to determine how much of the water column to exclude from the budget calculations.
444 The scatter indicates where air-sea exchange exerts an influence on water properties
445 (Supplementary Figure 3), and that part of the upper water column is excluded from budget
446 calculations that assume the only changes between inflow and outflow result from meltwater
447 addition.

448 The initial circulation, adjustments and final circulation derived using mid-range WW properties are
 449 shown for each section in Supplementary Figure 4, with analogous results from available directly-
 450 observed currents in Supplementary Figure 5. As the largest currents associated with the undesired
 451 high-frequency variability are likely to be approximately pressure-independent, an identical
 452 technique preserves the observed depth-dependent current structure, but closes budgets by adding
 453 depth-independent velocity adjustments calculated as described above. Prior de-tiding of the
 454 observed currents has a negligible impact on the results, because tidal currents near Dotson Ice Shelf
 455 are typically much smaller than the applied adjustments.

456 Since some underlying assumptions, particularly that of steady, geostrophic flow, will hold only
 457 approximately, any one solution will generally provide an unreliable estimate of the circulation and
 458 ice shelf melt rate. Indeed, applying all constraints can sometimes yield excessively noisy solutions,
 459 since we are forcing inherently noisy observations to fit our assumptions exactly. We therefore
 460 generate the inverse of the constraint matrix using a Singular Value Decomposition, and we use a
 461 truncated rather than a full-rank solution if the latter is excessively noisy⁴⁸. With at most three
 462 constraints, this amounts to a choice between three (full-rank) or two (truncated) singular vectors.
 463 The procedure is repeated for all realisations of the WW properties (Supplementary Table 2), and
 464 each solution scored based on three measures of solution credibility:

$$465 \quad \text{Score} = \frac{1}{3} \left\{ \left(1 - \min \left[1, \frac{v_{rms}^{adj}}{V_{rms}^{adj}} \right] \right) + \left(1 - \min \left[1, \frac{v_{max}^{adj}}{V_{max}^{adj}} \right] \right) + \left(1 - \min \left[1, \frac{\delta m}{\Delta M} \right] \right) \right\}$$

466 where the three criteria are the root-mean-square velocity adjustment, v_{rms}^{adj} ; the maximum
 467 absolute adjustment, v_{max}^{adj} ; the difference between the transport imbalance and the net flux of
 468 meltwater fraction across the section, δm . In each case we specify a tolerance beyond which the
 469 solution scores 0 for that criterion:

$$470 \quad V_{rms}^{adj} = 0.1 \text{ m s}^{-1}; \quad V_{max}^{adj} = 0.2 \text{ m s}^{-1}; \quad \Delta M = 20 \text{ Gt yr}^{-1}$$

471 with levels chosen to remove the influence of the majority of physically unreasonable solutions.
 472 Additionally, the score for any solution with a meltwater flux less than zero or a circulation greater
 473 than 2 Sv is set to zero regardless of the other criteria. All solutions are shown in Supplementary
 474 Figure 6, along with the score-weighted mean and score-weighted standard deviation that provide
 475 the final results plotted in Figure 4. Further results are summarised in Supplementary Table 3.

476 ***Theoretical relationship between meltwater flux and ocean temperature***

477 Melting at the base of an ice shelf cools and freshens the water near the ice base and creates a
 478 buoyant current that flows along the ice-ocean interface. The melt rate (m) is determined by the
 479 heat flux across the turbulent boundary layer created by current shear against the ice base, and can
 480 be quantified as⁴⁹:

481
$$m = \left\{ \frac{C_d^{1/2} \Gamma_{TS}}{(L_i - c_i T_{*i})/c} \right\} U T_*$$

482 where U is current speed, $T_* = T - T_f$, is temperature relative to the salinity-dependent freezing point
 483 at the depth of the ice shelf base, sometimes referred to as thermal driving, c is specific heat
 484 capacity, L latent heat of fusion, C_d drag coefficient, Γ_{TS} a heat exchange coefficient, and the subscript
 485 i indicates ice properties. If the drag and thermal exchange coefficients are assumed to be constant,
 486 the term in braces, which will be denoted M_0 , is approximately constant, as it depends only weakly
 487 on the ice temperature relative to the seawater freezing point.

488 Assuming the large-scale circulation to be in geostrophic balance, the speed of the buoyant
 489 boundary current relative to the lower layer of inflowing water, $\Delta U = U - U_{in}$, can be written⁵⁰:

490
$$\Delta U = \frac{g}{f} \sin \theta \Delta \rho$$

491 where g is gravity, f the Coriolis parameter, θ the slope of the ice shelf base relative to the
 492 horizontal and $\Delta \rho = (\rho - \rho_{in})/\rho_{in}$, the dimensionless density deficit in the boundary current. The
 493 transports in the lower, inflowing layer and the buoyant boundary current are approximately equal,

494 differing only because of the addition of meltwater to the latter, so if both layers are of similar
 495 thickness, the speed of the buoyant current can be approximated as:

$$496 \quad U \approx \frac{\Delta U}{2}$$

497 The properties of the boundary current must lie somewhere along the mixing line connecting the
 498 properties of the inflow with those of the ice (the green lines in Supplementary Figure 2), so the
 499 temperature and salinity differences are related by⁴²:

$$500 \quad \frac{(T - T_{in})}{(S - S_{in})} = \frac{T_{*in} + (L_i - c_i T_{*i})/c}{S_{in}}$$

501 Combining this expression with a linear equation of state:

$$502 \quad \Delta\rho = \beta_S(S - S_{in}) - \beta_T(T - T_{in})$$

503 and a linear equation for the freezing point at the depth of the ice shelf base as a function of salinity:

$$504 \quad (T_* - T_{*in}) = (T - T_{in}) - \lambda_1(S - S_{in})$$

505 leads to an expression for the density deficit in terms of the thermal driving deficit⁵⁰:

$$506 \quad \Delta\rho = (T_* - T_{*in}) \left\{ \frac{\beta_S S_{in} - \beta_T [T_{*in} + (L_i - c_i T_{*i})/c]}{T_{*in} + (L_i - c_i T_{*i})/c - \lambda_1 S_{in}} \right\}$$

507 Once again the term in braces, which will be denoted P_0 , is approximately constant because of the
 508 weak dependence on the ice and inflow temperatures and the small range in inflow salinity.

509 Thermal driving in the boundary current must be less than that in the inflow, but greater than zero
 510 (if the ice shelf base is melting), a condition that can be expressed as:

$$511 \quad T_* = \varepsilon T_{*in} \quad 0 < \varepsilon < 1$$

512 and combining all the above results leads to an expression for the melt rate that is a quadratic
 513 function of the inflow temperature:

514
$$m = M_0 \frac{g}{2f} \sin \theta P_0 \varepsilon (\varepsilon - 1) T_{*in}^2$$

515 The term ε can be related to the relative efficiency of mixing across the thermocline that separates
 516 the boundary current from the warmer water below and across the ice-ocean boundary layer. One
 517 way to estimate the magnitude of ε is to assume an approximate balance between the vertical
 518 turbulent heat fluxes that act to warm and cool, respectively, the boundary current^{34,49,51}. The
 519 former is often parameterised as a process of entrainment into the boundary current, whereby the
 520 entrainment rate is expressed as a function of the current speed and the boundary slope, while the
 521 latter is simply the heat flux that drives melting, defined above:

522
$$E_0 \Delta U \sin \theta (T_{*in} - T_*) \approx C_d^{1/2} \Gamma_{TS} U T_*$$

523 Both heat fluxes scale with the speed of the boundary current, in recognition of the fact that current
 524 shear drives the turbulent mixing. Using the above balance, the expression for ε becomes:

525
$$\varepsilon \approx \frac{2E_0 \sin \theta}{C_d^{1/2} \Gamma_{TS} + 2E_0 \sin \theta}$$

526 The neglect of heat advection within the boundary current in formulating the above balance of
 527 vertical turbulent fluxes is inappropriate when the inflow temperature is close to the surface
 528 freezing point and advection becomes critical in creating regions of basal freezing (where ε becomes
 529 negative). A pragmatic solution is to evaluate the thermal driving in the above theory relative to the
 530 surface freezing point and to define an offset at zero thermal driving, where the theory would give a
 531 melt rate of zero, from observations on ice shelves in cold oceanic environments, where a spatial
 532 average over regions of basal melting and freezing typically gives a small net melt rate²⁷.

533 Taking conventional values for physical constants ($g = 9.8 \text{ m s}^{-2}$, $f = -1.4 \times 10^{-4} \text{ s}^{-1}$, $L_i = 3.4 \times 10^5 \text{ J kg}^{-1}$, $c_i =$
 534 $2.0 \times 10^3 \text{ J kg}^{-1} \text{ K}^{-1}$, $c = 4.0 \times 10^3 \text{ J kg}^{-1} \text{ K}^{-1}$, $\theta_s = 7.9 \times 10^{-4}$, $\theta_T = 3.9 \times 10^{-5} \text{ K}^{-1}$, $\lambda_1 = -5.7 \times 10^{-2} \text{ K}$) and parameters
 535 ($E_0 = 3.6 \times 10^{-2}$, $C_d^{1/2} \Gamma_{TS} = 5.9 \times 10^{-4}$), choosing appropriate mean values for Dotson Ice Shelf ($S_{in} = 34.5$,
 536 $T_{*i} = -15^\circ\text{C}$, $\sin \theta = 8 \times 10^{-3}$), and defining a zero thermal driving offset of 0.5 m yr^{-1} , yields the curve

537 plotted in Figure 4c. The shading around that line indicates the range of curves obtained when the
538 parameters and input data for Dotson Ice Shelf are individually varied by $\pm 50\%$ (but $\pm 10\%$ in the case
539 of S_{in} , because known variations are small, and $\pm 100\%$ for the zero thermal driving offset).

540 **Data availability**

541 The oceanographic data that support the findings of this study are available in the U.S. Antarctic
542 Program Data Center (USAP-DC, <http://www.usap-dc.org/>), a member of the Interdisciplinary Earth
543 Data Alliance (IEDA), with the identifier <https://doi.org/10.15784/601105>. Raw and processed data
544 for individual cruises, along with details of the processing, can also be obtained upon reasonable
545 request from the points of contact listed in Supplementary Table 1.

546 **Code availability**

547 The Matlab scripts used for the analyses described in this study, along with data files formatted for
548 use with the software, can be obtained from the corresponding author upon reasonable request.

549

550 **References**

- 551 42. Jenkins, A. The impact of melting ice on ocean waters. *J. Phys. Oceanogr.* **29**, 2370–2381 (1999).
- 552 43. Millan, R., Rignot, E., Bernier, V., Morlighem, M. & Dutrieux, P. Bathymetry of the Amundsen Sea
553 Embayment sector of West Antarctica from Operation IceBridge gravity and other data, *Geophys.*
554 *Res. Lett.* **44**, 1360–1368 (2017).
- 555 44. Jenkins, A. et al. Observations beneath Pine Island Glacier in West Antarctica and implications
556 for its retreat. *Nature Geosci.* **3**, 468–472 (2010).
- 557 45. Biddle, L.C., Heywood, K.J., Kaiser, J. & Jenkins, A. Glacial Meltwater Identification in the
558 Amundsen Sea, *J. Phys. Oceanogr.* **47**, 933–954 (2017).

- 559 46. Nakayama, Y, Schröder, M. & Hellmer, H.H. From circumpolar deep water to the glacial
560 meltwater plume on the eastern Amundsen Shelf. *Deep-Sea Res. Part I* **77**, 50–62 (2013).
- 561 47. Jenkins, A. & Jacobs, S.S. Circulation and melting beneath George VI Ice Shelf, Antarctica. *J.*
562 *Geophys. Res.* **113**, C04013 (2008).
- 563 48. Wunsch, C. The North Atlantic general circulation west of 50°W determined by inverse methods.
564 *Rev. Geophys. Space Phys.* **16**, 583–620 (1978).
- 565 49. Jenkins, A. Convection-driven melting near the grounding lines of ice shelves and tidewater
566 glaciers. *J. Phys. Oceanogr.* **41**, 2279–2294 (2011).
- 567 50. Jenkins, A. A simple model of the ice shelf–ocean boundary layer and current. *J. Phys. Oceanogr.*
568 **46**, 1785–1803 (2016).
- 569 51. Little, C.M., Gnanadesikan, A. & Oppenheimer, M. How ice shelf morphology controls basal
570 melting. *J. Geophys. Res.* **114**, C12007 (2009).

Supplementary Information

for

**West Antarctic Ice Sheet retreat in the Amundsen Sea driven by decadal
oceanic variability**

Adrian Jenkins^{1*}, Deb Shoosmith¹, Pierre Dutrieux², Stan Jacobs², Tae Wan Kim³,
Sang Hoon Lee³, Ho Kyung Ha⁴ & Sharon Stammerjohn⁵

¹*British Antarctic Survey, Natural Environment Research Council, Cambridge CB3 0ET, U.K.*

²*Lamont-Doherty Earth Observatory of Columbia University, Palisades, NY 10964, U.S.A.*

³*Korea Polar Research Institute, Incheon 406-840, Korea.*

⁴*Department of Ocean Sciences, Inha University, Incheon 22212, Korea.*

⁵*Institute of Arctic and Alpine Research, University of Colorado, Boulder, CO 80309, U.S.A.*

Supplementary Table 1 | Details of datasets used.

Year	Cruise Number	Ship	Contact	E-mail	Station numbers (west to east)	Dates	Instruments
2000	NBP0001	Nathaniel B Palmer	Jacobs	sjacobs@ldeo.columbia.edu	53, 54, 55	3-4 March 2000	CTD, DO, LADCP
2006	JR141	James Clark Ross	Jenkins / Shoosmith	ajen@bas.ac.uk	18, 17, 16, 15, 14, 13	30 Jan 2006	CTD
2007	NBP0702	Nathaniel B Palmer	Jacobs	sjacobs@ldeo.columbia.edu	64, 65, 66, 67, 68, 69	22-23 Feb 2007	CTD, DO, LADCP
2009	NBP0901	Nathaniel B Palmer	Jacobs	sjacobs@ldeo.columbia.edu	119, 120, 121, 122, 123, 124	4-5 Feb 2009	CTD, DO, LADCP
2011	NBP1005	Nathaniel B Palmer	Stammerjohn	sharon.stammerjohn@colorado.edu	29, 10, 11, 9	17 Dec 2010; 2 Jan 2011	CTD, DO
2012	ANA02C	Araon	Kim / Lee	twkim@kopri.re.kr	2701, 2801, 1901, 2001, 2101	16-18 Feb 2012	CTD, DO
2014	ANA04	Araon	Kim / Lee	twkim@kopri.re.kr	1026, 1025, 1024, 1023, 1022	8-9 Jan 2014	CTD, DO, LADCP
2016	ANA06	Araon	Kim / Lee	twkim@kopri.re.kr	221, 211, 201, 191, 181, 172	19-20 Jan 2016	CTD, DO, LADCP

Instruments are Conductivity-Temperature-Depth sensors (CTD), Dissolved Oxygen sensors (DO) and Lowered Acoustic Doppler Current Profilers (LADCP).

Supplementary Table 2 | End member properties used to calculate meltwater fraction for each year.

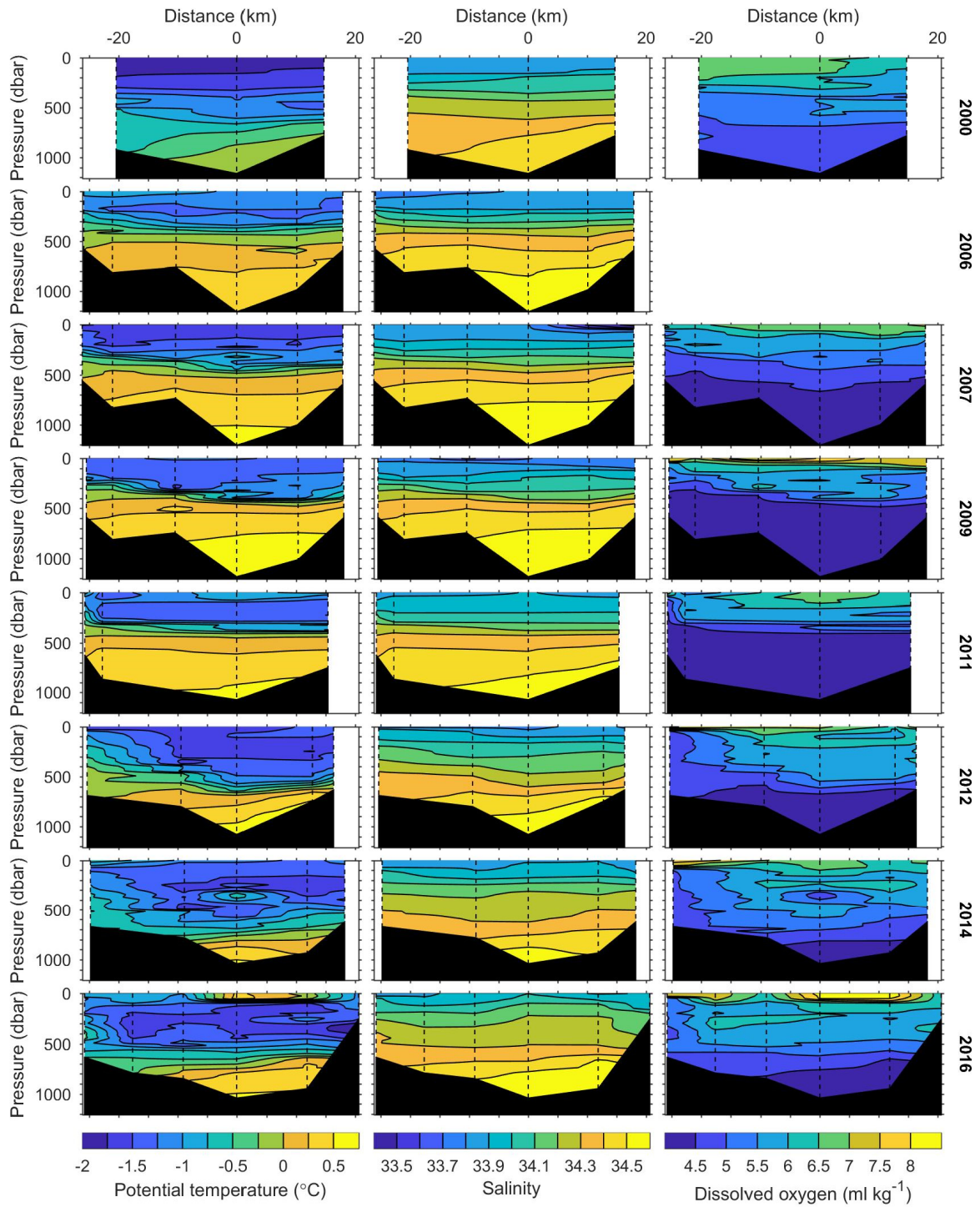
Year	Ice properties			mCDW properties			WW properties		
	T	S	DO	T	S	DO	T	S	DO
2000	-95	0	24.5	-0.3	34.43	4.75	$T_{fp}(S)$	34.22 – {0, 0.03, 0.06, 0.09}	$DO_{sat}(S, T) –$ {0, 0.5, 1, 1.5, 2, 2.5, 3}
2006	-95	0		0.75	34.63		$T_{fp}(S)$	34.07 – {0, 0.065, 0.13, 0.195}	$DO_{sat}(S, T) –$ {0, 0.5, 1, 1.5, 2, 2.5, 3}
2007	-95	0	24.5	0.8	34.62	4.36	$T_{fp}(S)$	34.18 – {0, 0.09, 0.18, 0.27}	$DO_{sat}(S, T) –$ {0, 0.5, 1, 1.5, 2, 2.5, 3}
2009	-95	0	24.5	1.0	34.65	4.225	$T_{fp}(S)$	34.1 – {0, 0.05, 0.1 0.15}	$DO_{sat}(S, T) –$ {0, 0.5, 1, 1.5, 2, 2.5, 3}
2011	-95	0	24.5	0.85	34.61	4.05	$T_{fp}(S)$	34.15 – {0, 0.06, 0.12, 0.18}	$DO_{sat}(S, T) –$ {0, 0.5, 1, 1.5, 2, 2.5, 3}
2012	-95	0	24.5	0.56	34.545	4.15	$T_{fp}(S)$	34.2 – {0, 0.035, 0.07, 0.105}	$DO_{sat}(S, T) –$ {0, 0.5, 1, 1.5, 2, 2.5, 3}
2014	-95	0	24.5	0.0	34.45	4.5	$T_{fp}(S)$	34.23 – {0, 0.02, 0.04, 0.06}	$DO_{sat}(S, T) –$ {0, 0.5, 1, 1.5, 2, 2.5, 3}
2016	-95	0	24.5	0.025	34.47	4.55	$T_{fp}(S)$	34.25 – {0, 0.015, 0.03, 0.045}	$DO_{sat}(S, T) –$ {0, 0.5, 1, 1.5, 2, 2.5, 3}

Properties are potential temperature (T in °C), practical salinity (S) and concentration of dissolved oxygen (DO in ml kg⁻¹). Ice properties are: an effective potential temperature that implicitly incorporates the heat loss associated with warming the ice by 15°C from its core temperature to the seawater freezing point, then melting it⁴²; a practical salinity of 0; a dissolved oxygen concentration that assumes the ice is formed from the compaction of cold firn at elevations of 1000–2000 m above sea level⁴⁷. Properties of mCDW come from observation, while those of WW are derived from an assumed salinity, with subscripts fp and sat indicating, respectively, the freezing point at atmospheric pressure as a function of salinity and the saturation concentration at atmospheric pressure as a function of salinity and potential temperature. For each year 28 realisations of WW properties are created by subtracting the values in braces from the maxima (shown graphically in Supplementary Figure 2).

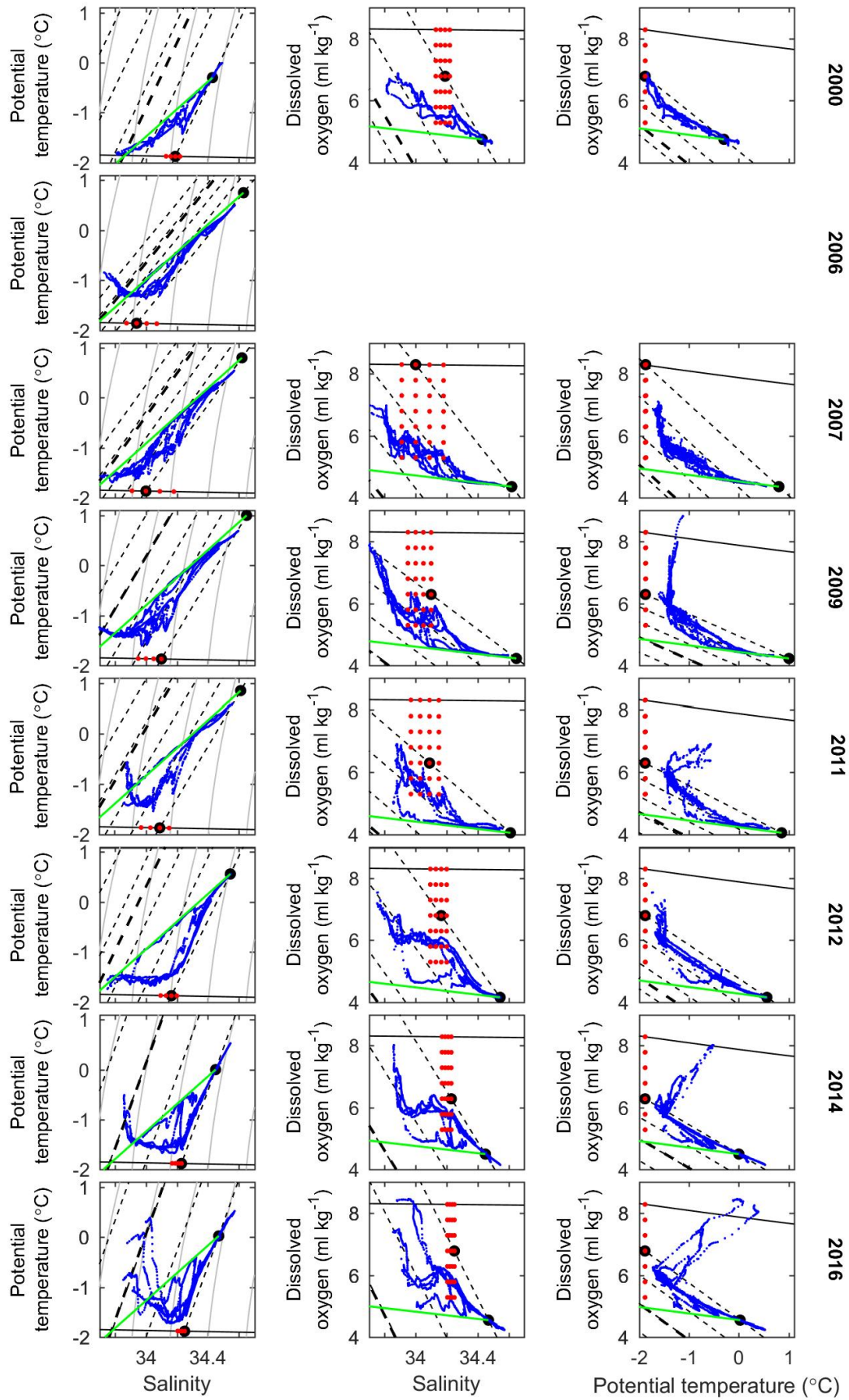
Supplementary Table 3 | Score-weighted mean and standard deviation for key diagnostics of the circulation across Dotson Ice Front in each year.

Year	2000	2006	2007	2009	2011	2012	2014	2016
Geostrophic solutions								
Number and type (F/T)	21 (F)	8 (F)	55 (F)	28 (T)	56 (T)	56 (F)	19 (T)	20 (F)
Mean inflow properties								
Transport (Sv)	1.17	0.39	0.61	0.71	0.46	0.64	0.83	0.79
STD (Sv)	0.28	0.05	0.19	0.37	0.07	0.06	0.12	0.24
Temperature (°C)	1.14	1.89	1.63	2.06	1.98	1.20	0.92	0.89
STD (°C)	0.09	0.19	0.19	0.22	0.12	0.27	0.04	0.13
Meltwater fraction (permille)	2.2	2.3	5.7	4.9	3.7	3.6	3.4	4.1
STD (permille)	1.0	0.9	1.9	1.8	1.1	2.3	1.2	1.5
Mean section properties								
Net transport (Gt yr ⁻¹)	31.0	65.6	31.0	88.2	51.5	20.9	23.1	20.5
STD (Gt yr ⁻¹)	2.5	5.1	10.8	23.4	7.0	3.3	6.9	10.8
Net melt transport (Gt yr ⁻¹)	20.8	45.9	33.8	97.2	56.2	19.7	30.6	18.5
STD (Gt yr ⁻¹)	4.4	10.1	16.7	30.8	9.8	5.1	7.8	10.9
Temperature (°C)	1.07	1.59	1.54	1.87	1.67	1.16	0.97	1.02
STD (°C)	0.09	0.10	0.20	0.20	0.15	0.14	0.02	0.03
LADCP solutions								
Number and type (F/T)	24 (F)		40 (T)	28 (T)			28 (T)	
Mean inflow properties								
Transport (Sv)	0.99		1.17	0.72			0.51	
STD (Sv)	0.46		0.49	0.18			0.09	
Temperature (°C)	1.15		1.70	2.20			1.14	
STD (°C)	0.09		0.34	0.13			0.06	
Meltwater fraction (permille)	1.7		4.9	4.2			2.0	
STD (permille)	1.2		1.6	1.0			1.2	
Mean section properties								
Net transport (Gt yr ⁻¹)	24.9		82.1	81.5			16.7	
STD (Gt yr ⁻¹)	6.1		21.9	12.7			3.3	
Net melt transport (Gt yr ⁻¹)	23.8		90.8	99.6			20.5	
STD (Gt yr ⁻¹)	8.1		37.9	17.3			2.9	
Temperature (°C)	1.12		1.64	1.85			1.02	
STD (°C)	0.10		0.25	0.18			0.08	

Number and type (F=full, T=truncated) of solutions with non-zero scores that contribute to the mean and standard deviation for each year. Geostrophic and LADCP solutions are shown separately above, but are combined in Supplementary Figure 6. Mean inflow properties are evaluated over all areas of the section where the inferred current is into the cavity, while mean section properties are evaluated over inflow and outflow regions. The near-surface layer where air-sea interactions affect properties (Supplementary Figure 3) was excluded from the calculations of circulation and property means. In cases where only a small region was excluded, calculations were repeated including the full water column from the sea surface down to the seabed, giving a maximum of 56 possible solutions for those sections. Temperatures are relative to the surface freezing point.

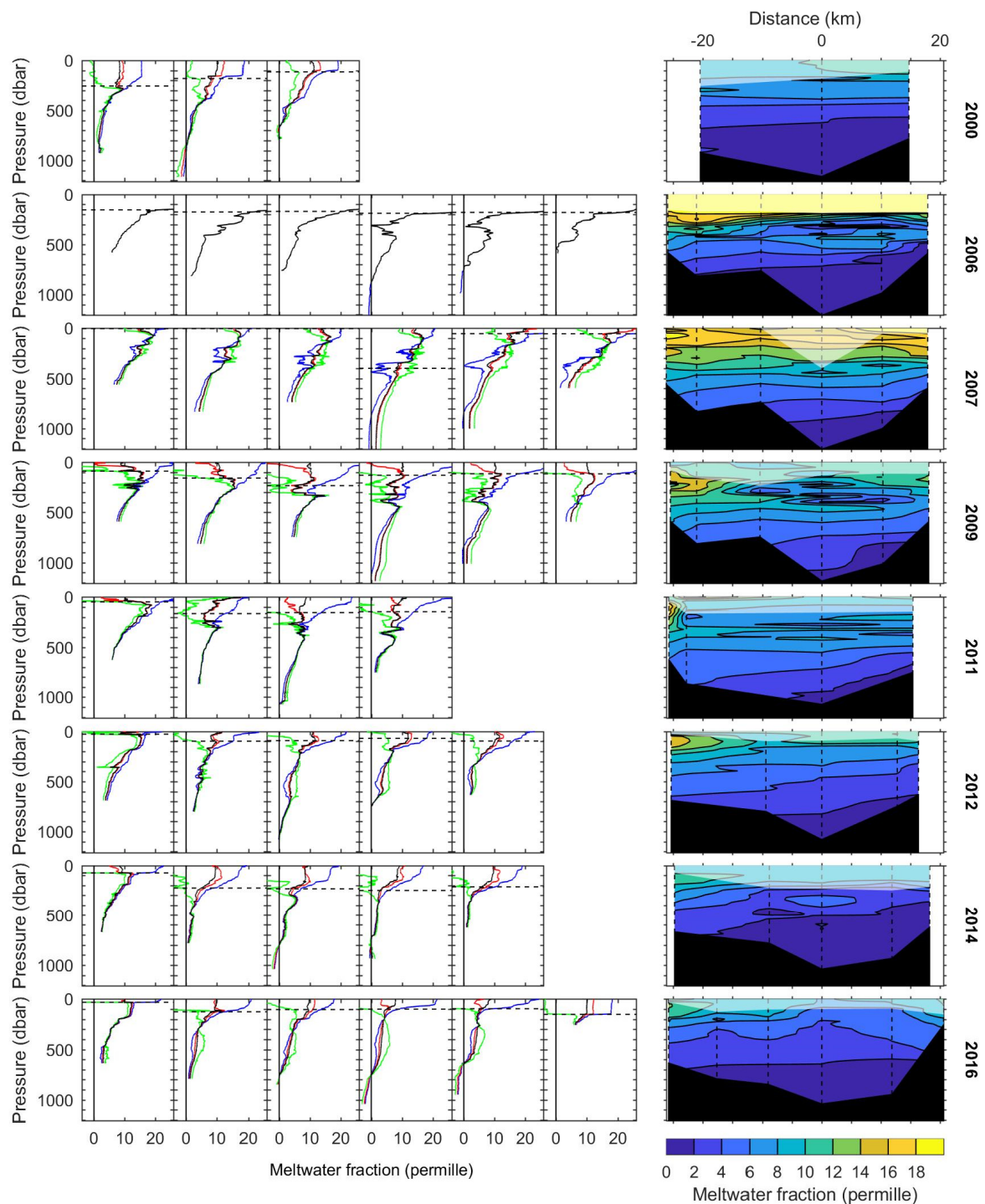


Supplementary Figure 1 | Cross-sections of potential temperature, salinity and dissolved oxygen concentration measured at Dotson Ice Front. Station locations are indicated by vertical dashed lines, with the year of observation on the right (Supplementary Table 1 has precise dates). Distance relative to the central trough station is positive eastward, and black shading shows the seabed, linearly interpolated between stations. Dissolved oxygen (right) was not measured in 2006.

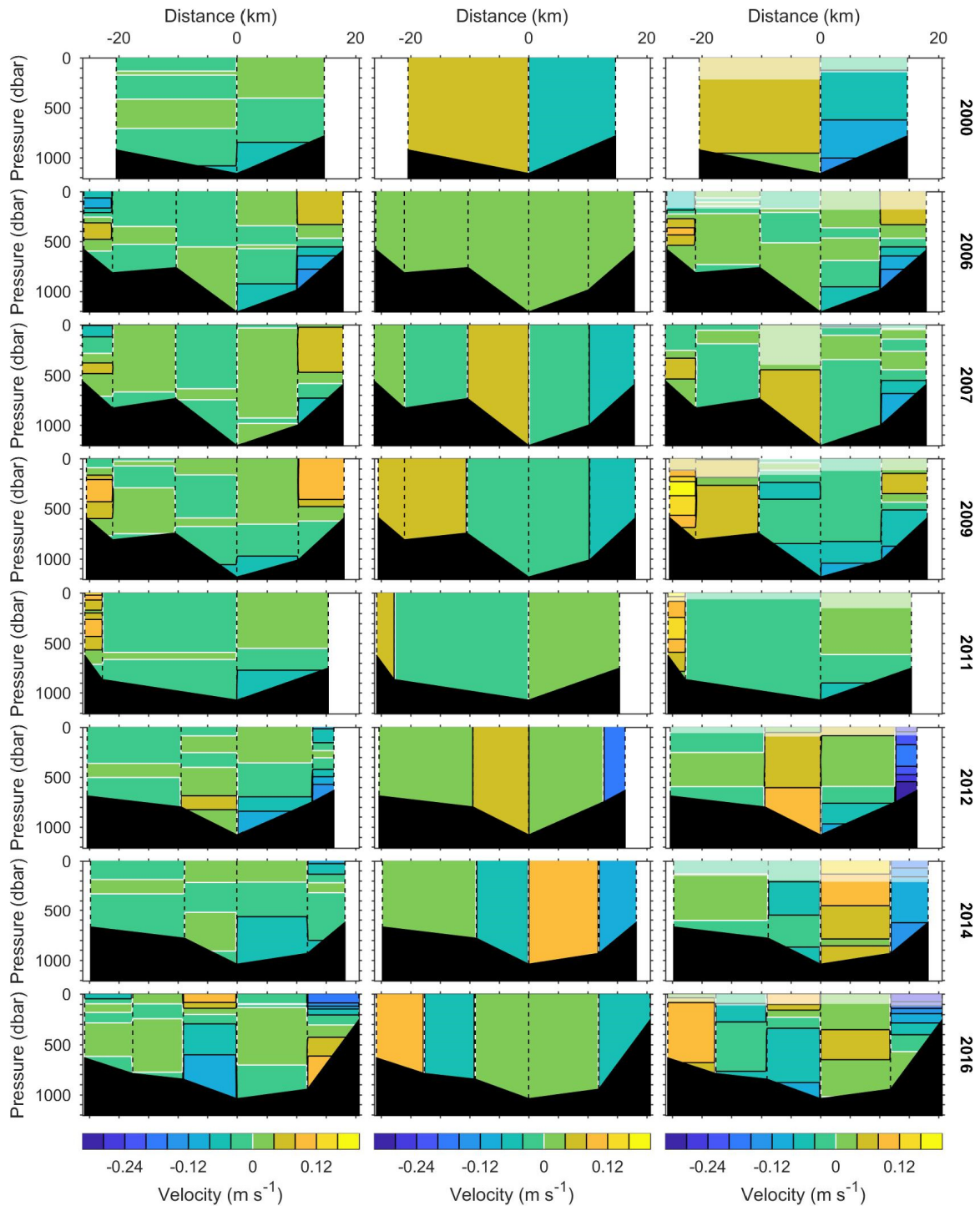


Supplementary Figure 2 | Scatter plots of potential temperature, salinity and dissolved oxygen concentration measured at Dotson Ice Front. Blue dots are 1 dbar averages from each vertical profile,

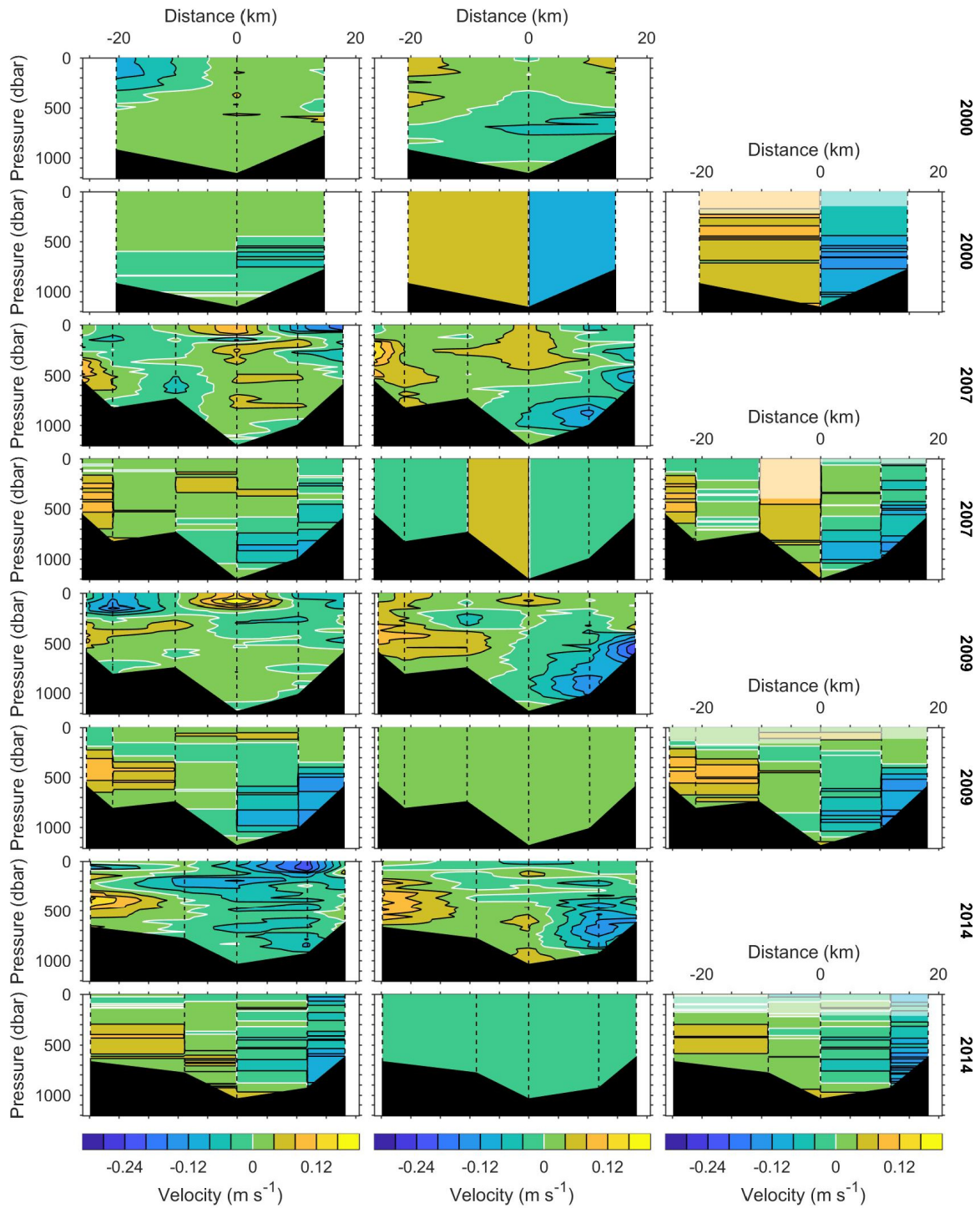
with the year of observation on the right. Dissolved oxygen was not measured in 2006. Solid black lines show the freezing point temperature (left-hand panels) and saturation concentration (centre and right-hand panels) at atmospheric pressure, while solid grey lines (left-hand panels) are contours of potential density (1027 to 1027.8 kg m⁻³ in 0.2 kg m⁻³ increments). Red dots indicate WW properties used in calculations of meltwater fraction and transport (Methods and Supplementary Table 2). Black circles are the mCDW properties (Supplementary Table 2) and the particular WW properties used to calculate contours of meltwater fraction (dashed, black lines, 0 to 40 permille in 10 permille increments) and results in Supplementary Figures 3, 4 and 5. Green lines connect mCDW properties and (assumed constant) ice properties⁴² (Supplementary Table 2). Bold, dashed, black lines are the theoretical upper bounds of meltwater fraction (intersection of green and freezing point lines)⁴².



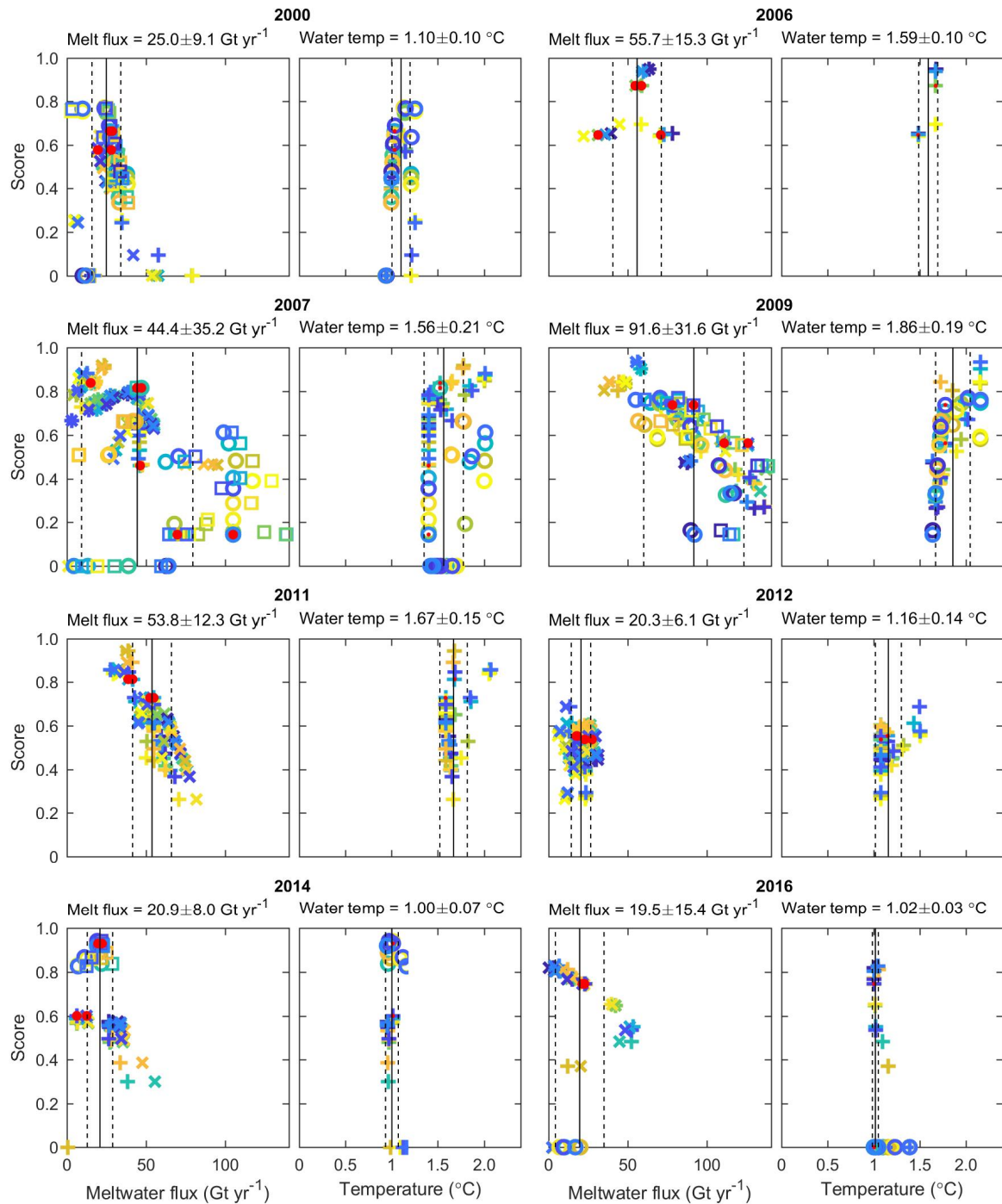
Supplementary Figure 3 | Individual station profiles and resulting cross-sections of meltwater fraction from observations at Dotson Ice Front. Three estimates of meltwater fraction (Methods and Supplementary Figure 2) are based on potential temperature and salinity (blue profiles), dissolved oxygen and salinity (red profiles) and dissolved oxygen and potential temperature (green profiles). Black profiles show the mean of those estimates (only one is possible in 2006), used to produce the contoured cross-sections (right). Dashed horizontal lines on profile plots and lighter shading on cross-sections indicate where meltwater fractions are disregarded because air-sea interactions affect near-surface properties. Horizontal distance axis origin and direction as in prior figure; individual station profiles also from west (left) to east (right).



Supplementary Figure 4 | Geostrophic currents perpendicular to Dotson Ice Front. Geostrophic currents between each station pair (left-hand panels) calculated using the slope of the isobars, determined from temperature and salinity profiles (Supplementary Figure 1), and an assumption of zero velocity at the lowest level in the water column with a significant meltwater fraction (Methods, Supplementary Figure 3). Depth-independent velocity adjustments (centre panels) are the minimum additions required for the resulting geostrophic circulation (right-hand panels) to satisfy integral constraints on the net transport of heat, salt and dissolved oxygen (Methods, particular solution plotted was obtained using WW properties indicated in Supplementary Figure 2). Positive values indicate flow away from the ice (northward), with lighter shading (right-hand panels) indicating the near-surface layer excluded from the calculations because of the impact of air-sea interaction.



Supplementary Figure 5 | Directly-measured currents perpendicular to Dotson Ice Front in 2000, 2007, 2009 and 2014. In each summer, zonal (left) and meridional (right) Lowered Acoustic Doppler Current Profiler components are shown in the upper two panels. The lower three panels show mean currents perpendicular to the ice front between each station pair (left) and minimum depth-independent velocity adjustments (centre) required for the resulting circulation (right) to satisfy integral constraints on the net transport of heat, salt and dissolved oxygen (Methods, particular solution plotted was obtained using WW properties indicated in Supplementary Figure 2). Positive values and lighter shading (right) as in previous figure. LADCP data in 2016 sampled a strong transient, depth-independent flow at one station, preventing any solutions with scores above zero (Methods and Supplementary Figure 6).



Supplementary Figure 6 | Meltwater flux and mean temperature above the surface freezing point across Dotson Ice Front. Results obtained for each choice of WW properties (Supplementary Table 2 and Supplementary Figure 2) are plotted (colour-coded) against the score for that solution (Methods). Solutions derived from geostrophic currents are indicated by crosses (+ and x), and those from LADCP data by circles and squares. On plots of meltwater flux, crosses (+) and circles indicate the difference between inflow and outflow, and crosses (x) and squares the net meltwater flux (Methods). Red dots denote solutions obtained with WW properties highlighted in Supplementary Figure 2 and used in Supplementary Figures 3, 4 and 5. Score-weighted means and standard deviations are indicated by vertical solid and dashed lines, respectively, and are noted numerically above each plot. Mean temperatures are averaged over the relevant section area included in the constrained budget calculation. Final score-weighted results are used in Figure 4 of the main text.